Self-assembly of multi-component mitochondrial nucleoids via phase separation

Marina Feric[1,2], Tyler G. Demarest[3], Jane Tian[3], Deborah L. Croteau[3], Vilhelm A. Bohr[3], and Tom Misteli[1,*]

[1]National Cancer Institute, NIH, Bethesda, MD, USA.

[2]National Institute of General Medical Sciences, NIH, Bethesda, MD, USA.

[3]National Institute on Aging, NIH, Baltimore, MD, USA.

*Correspondence to: mistelit@mail.nih.gov

Abstract

Mitochondria contain an autonomous and spatially segregated genome. The organizational unit of mitochondrial genomes is the nucleoid, which consists of mitochondrial DNA (mtDNA) and associated architectural proteins. The physical properties and mechanisms of assembly of mitochondrial nucleoids and how they contribute to disease remain largely unclear. Here, we show that phase separation is the primary physical mechanism for assembly of mitochondrial nucleoids, and we demonstrate enrichment of enlarged, droplet-like nucleoids in mitochondria from patients with the premature aging disorder Hutchinson-Gilford Progeria Syndrome (HGPS). Mitochondrial nucleoids exhibit morphological features, coarsening behavior, and dynamics of phase-separated structures *in vitro* and *in vivo*. The major mtDNA-binding protein TFAM spontaneously phase separates *in vitro* into viscoelastic droplets with slow internal dynamics, and the combination of TFAM and mtDNA is sufficient to promote the *in vitro* formation of multiphase structures with gel-like properties, which recapitulate the *in vivo* behavior of mitochondrial nucleoids in live human cells. Altered mitochondrial nucleoid structure in HGPS is accompanied by local enrichment of mitochondrial unfolded protein response (UPR^{mt}) markers and mitochondrial dysfunction. These results identify phase separation as the physical mechanism driving the organization of mitochondrial nucleoids, with ramifications for mitochondrial function.

Main Text

Mitochondria are the major sites of cellular energy production through oxidative phosphorylation and generation of ATP. Within each mammalian cell, mitochondria contain several hundred copies of a 16.6 kb circular genome[1,2]. Unlike the nuclear genome, mitochondrial DNA (mtDNA) is not organized by histones, but is packaged by a distinct set of proteins into nucleoprotein complexes to form mitochondrial nucleoids (mt-nucleoids)[2,3]. These structures are typically uniformly ~100 nm in size and lack delimiting membranes[4,5]. The major mt-nucleoid packaging factor in human cells is the mitochondrial transcription factor A (TFAM)[2], which binds and compacts mtDNA *in vitro* into nucleoid-like structures[6-8].

Mitochondrial defects are prominently linked to cellular and organismal aging as mitochondria are the main producers of reactive oxygen species (ROS) in the cell[9,10], and the generation of an oxidative cellular environment during aging is thought to be deleterious to mitochondrial function as well as to their genomes[11,12]. Moreover, mtDNA mutations accumulate during normal aging[10,13], and elevated mutation levels of mtDNA cause premature aging phenotypes[14,15]. Beyond the direct binding of TFAM to mtDNA, it remains largely unknown how the higher-order morphological features of the mitochondrial genome emerge and affect function, and whether anomalies in mt-nucleoids contribute to disease.

To test if structural changes to mt-nucleoids are associated with disease, we investigated their organization in the rare premature aging disorder Hutchinson-Gilford Progeria Syndrome (HGPS)[16]. We detected prominently enlarged mt-nucleoids and accumulation of TFAM in multiple skin fibroblast cell lines from advanced HGPS patients compared to control lines (Fig. 1, Extended Data Fig. 1)[17,18]. High-throughput spinning-disc confocal microscopy revealed mitochondria with typically tubular, elongated shapes, forming interconnected networks throughout the cytoplasm in control cells (Fig. 1a, Extended Data Fig. 1e,f), whereas ~70% of advanced HGPS patient cells had a sub-population of mitochondria that were swollen, spherical in shape and isolated from the surrounding mitochondrial network (Fig. 1b, Extended Data Fig. 1g-k). The extent and number of enlarged mitochondria correlated with disease

progression and damaged mitochondria were also sporadically observed in control cells (Fig. 1c, Extended Data Fig. 1k).

Analysis of enlarged mitochondria by high-resolution Structured Illumination Microscopy (SIM) imaging revealed that, in morphologically aberrant mitochondria, mt-nucleoids clustered together into structures that were considerably brighter and larger than the typically uniform 100 nm nucleoids found in normal mitochondria (Fig. 1d-g). Several mt-nucleoid markers, including mtDNA and the major mtDNA-packaging protein, TFAM, were locally enriched in the atypical mitochondria (Fig. 1f,g; Extended Data Fig. 1o,p), while total TFAM and mtDNA levels were not altered in HGPS cells (Extended Data Fig. 1l-n). In addition, several chaperones and proteases of the mitochondrial unfolded protein response (UPR^{mt}) including HSPD1 (mtHSP60), mtHSP10, mtHSP70, ClpP, and LONP1, were 1.5-2 fold enriched in enlarged mitochondria relative to levels in normal, tubular mitochondria (Fig. 1j-l; Extended Data Fig. 1q-v). Exogenous expression of progerin, the disease-causing isoform of lamin A in HGPS, was sufficient to induce in wild-type cells an increase in the number of morphologically damaged mitochondria that scaled with progerin expression and defects in nuclear shape and was similar to the increase observed in patient cells (Extended Data Fig. 2). These observations document in HGPS patient cells a significant enrichment of morphologically aberrant, enlarged mitochondria, which exhibit hallmarks of mitochondrial stress.

These findings prompted us to explore the molecular mechanism involved in formation of mt-nucleoids and their enlargement. Mitochondrial nucleoids are known to undergo frequent fusion and fission events *in vivo*[19], and enlargement and remodeling of mt-nucleoids are prominent cellular responses to stress, including after exposure to DNA intercalating agents or phototoxic stress[20]. To characterize the nucleoid enlargement process *in vivo*, we exposed primary skin fibroblasts to phototoxic stress[21] (see Supplementary Information). Live-cell imaging captured the rapid contraction of mitochondria accompanied by pronounced fusion events between neighboring mt-nucleoids to generate enlarged droplet-like structures greater than 100 nm in size and up to a few microns in diameter, similar to those

seen in damaged, swollen mitochondria of HGPS cells (Fig. 1h,i and Supplementary Videos 1 and 2). Similar, but even more pronounced, fusion events were observed in the presence of the intercalator EtBr (Supplementary Videos 3 and 4). These results suggest that loss of mitochondrial homeostasis results in the inability to maintain a homogenous nucleoid size of ~100 nm. The observed enlargement of nucleoids by fusion and the dynamics of viscous behavior and mt-nucleoid coalescence (Fig. 1h,i, Supplementary Videos 1-4), are consistent with properties of liquid droplets and are reminiscent of phase separation processes observed in non-membrane bound cellular bodies[22].

Numerous ribonucleoprotein and nucleoprotein complexes spontaneously self-assemble into non-membrane bound cellular bodies, or biomolecular condensates, via liquid-liquid phase separation[23,24]. The canonical examples of RNA-protein bodies include the nucleolus in the nucleus[25,26] as well as P-granules[27] and stress granules[28] in the cytoplasm. In addition, DNA-protein complexes can phase separate, such as the heterochromatin protein HP1α in the context of heterochromatin[29,30], histones to form chromatin domains[31,32], or super-enhancers which form active transcriptional hubs[33]. To explore if liquid-liquid phase separation drives mt-nucleoid assembly, we investigated the ability of the major, highly abundant nucleoid packaging protein TFAM to undergo phase separation *in vitro*. TFAM phase separated into spherical droplets in low salt conditions and at protein concentrations of ≥5 μM TFAM (Fig. 2a, Extended Data Fig. 3d). Droplet formation was reversible upon increasing salt concentration (Extended Data Fig. 3e). After 30-60 min post-mixing, droplets coarsened to sizes of ~1-5 μm and sedimented towards the bottom of the imaging chamber (Fig. 2a). The TFAM concentrations required for phase separation *in vitro* were well within the estimated physiological range inside the mitochondria of ~10 μM (see Supplementary Information)[4].

We performed a series of biophysical assays on TFAM droplets to assess their material properties within the first 30-90 minutes after mixing. Photobleaching of a $R \approx 0.5\ \mu m$ spot revealed slow dynamics with a characteristic time scale of $\tau \approx 6.5 \pm 0.5$ minutes, which corresponded to a diffusivity of $\sim 6 \times 10^{-4}\ \mu m^2/s$. Furthermore, the immobile fraction of 0.5±0.2 was indicative of viscoelastic behavior (Fig.

2b, Supplementary Video 5). Similarly, time-lapse images of TFAM droplets undergoing coalescence events also displayed slow dynamics with time scales of τ=4±0.5 min, giving rise to an inverse capillary velocity of 80±20 s/μm (Fig. 2c). Although the droplets had the propensity to relax upon contact, the average aspect ratio upon fusion was 1.36±0.04, which deviated from that of a sphere (AR=1.0) (Extended Data Fig. 3f). Introduction of dextran-FITC of varying sizes as an inert probe to sample the physicochemical environment of the droplets demonstrated that small particles of ≤1 nm preferentially accumulate within the droplets, while increasing probe size resulted in reduced partitioning (Fig. 2d). These properties are indicative of a characteristic pore or mesh size of ~1 nm, suggesting the presence of a polymer meshwork forming amongst individual TFAM molecules within the droplets. These biophysical properties suggest that TFAM molecules form an entangled polymer meshwork or gel with markedly slow internal arrangements and signatures of viscoelasticity.

To dissect the molecular features of TFAM responsible for phase separation, a set of TFAM mutants was analyzed for their phase separation behavior *in vitro*. TFAM contains two DNA-binding High Mobility Group (HMG) domains separated by a disordered linker domain and flanked by an intrinsically disordered C-tail, together forming a relatively flexible chain (Extended Data Fig. 3a)[34,35]. Additionally, TFAM is one of the most highly charged proteins in the mt-nucleoid (Extended Data Fig. 3c) and is primarily enriched in positive amino acids distributed throughout the length of the protein (Extended Data Fig. 3b). In phase separation assays, the HMGA domain alone failed to form the typical micron-sized droplets as seen with full-length TFAM, but assembled into small puncta near the diffraction limit even at high concentrations (Fig. 2f,g, Extended Data Fig. 3g,h). Maintaining half of the protein, either by adding a linker to HMGA (HMGA+linker) or with the analogous HMGB+C-tail mutant, restored droplet formation, albeit at higher saturation concentrations than full length TFAM, suggesting that multivalency seen in the full-length protein lowers the barrier for phase separation and that the addition of a disordered domain to HMGA promotes phase separation (Fig. 2f,g, Extended Data Fig. 3g,h). Loss of the disordered C-tail (ΔC-tail) did not affect phase separation, but influenced the wetting behavior of the droplets as

indicated by a decreased smoothness along the droplet perimeter (Fig. 2f,g, Extended Data Fig. 3g,h), indicating that the disordered C-tail regulates the molecular interactions within the droplet phase. Consistently, removal of the HMGA domain (ΔHMGA), also resulted in droplet formation, but at slightly higher saturation concentrations. Finally, introduction of six non-polar residues in the linker region (L6 mutant), based on the TFAM crystal structure[35], enhanced the gel-like properties of droplets as evidenced by the highly non-spherical morphologies whereas inclusion of non-polar residues in the HMGA domain to prevent dimerization[35] (no dimer mutant) increased saturation concentrations and produced relatively smaller droplets, underscoring the contribution of multivalent interactions in phase separation of TFAM (Fig. 2f,g, Extended Data Fig. 3g,h). Taken together, these observations suggest a mechanism by which many weak interactions along a flexible backbone of TFAM allow for robust phase separation and that the disordered linker and C-tail provide flexibility of the biopolymer chain to promote phase separation into prominent droplets.

To examine the interplay of mtDNA and TFAM in phase separated mt-nucleoids as would occur in the context of mitochondria, we investigated the *in vitro* phase separation behavior of TFAM in the presence of mtDNA (Fig. 3; Extended Data Fig. 4a,b). As expected, mtDNA (0-10 nM or equivalently 0-100 ng/ul) on its own did not phase separate, but when combined with TFAM at concentrations that support phase separation (≥5 μM), mtDNA readily partitioned into droplets. Importantly, the presence of mtDNA significantly affected droplet formation and morphology (Fig. 3a, Extended Data Fig. 4c). At a DNA/TFAM molar ratio of ~0.001, which corresponds to estimates of their physiological ratio[4] (see Supplementary Information), TFAM and mtDNA readily formed droplets (Fig. 3a, Extended Data Fig. 4c). At high mtDNA/TFAM molar ratios of >0.001, droplets ceased to form, potentially due to saturation behavior (Fig. 3a, Extended Data Fig. 4c). For molar ratios of mtDNA/TFAM ≤6E-4, the aspect ratio of the droplets notably increased with increasing ratio of DNA/TFAM mass concentrations (Fig. 3b). For mtDNA/TFAM molar ratios <3E-4, the number of droplets (measured approximately ~1 hour after mixing) increased with increasing mtDNA/TFAM levels (Fig. 3b inset), suggesting that mtDNA can

potentiate droplet formation under those conditions, possibly acting as a nucleating agent and paralleling how RNA drives phase separation when added to RNA-binding proteins[36]. ssDNA, dsDNA, and RNA as well as free nucleotides (dNTPs) also supported TFAM droplet formation (Extended Data Fig. 4d-s). Interestingly, ssDNA and dsDNA, considerably longer than the 16.6 kB mtDNA and with no sequence specificity, resulted in even more irregular droplet morphologies and pronounced gelation (Extended Data Fig. 4d-s). We conclude that the addition of long, polymerized strands of DNA, irrespective of sequence, leads to favorable interactions between TFAM and DNA, thereby affecting the emergent droplet behavior (Extended Data Fig. 4d-u). These findings demonstrate that the material properties of the droplets depend on DNA/TFAM composition where increasing DNA promotes gelation.

To probe how mtDNA localizes within the droplets, we performed SIM imaging on TFAM-mtDNA droplets containing increasingly higher concentrations of mtDNA. mtDNA is not uniformly distributed, but de-mixes from the majority of TFAM within the droplet (Fig. 3c-g), consistent with multiphase behavior seen in other multi-component phase separating systems, such as the nucleolus[25]. Multiphase organization was observed with both ssDNA and dsDNA, but not with dNTPs nor RNA (Extended Data Fig. 4j-s). To characterize the dynamics of multiphase TFAM-mtDNA droplets, fluorescence recovery after photobleaching (FRAP) demonstrated that TFAM was able to diffuse within TFAM-mtDNA droplets with similar recovery behavior as in pure TFAM droplets (Fig. 3h,j, Supplementary Video 6). In contrast, on these timescales, mtDNA within the droplets remained strikingly immobile (Fig. 3i,j, Supplementary Video 6), suggesting that the mtDNA molecules within the TFAM-mtDNA droplets determine the time scale for relaxation of the droplets, while also explaining the observed non-spherical shapes at high mtDNA/TFAM ratios. The observed dynamics are consistent with the multiphase sub-structure of these droplets.

To test if the *in vitro* phase-separation behavior of TFAM and mtDNA reflects the dynamic properties and structural organization of nucleoids *in vivo*, we visualized mt-nucleoids in HeLa cells using TFAM-mKate2. In photobleaching experiments, TFAM-mKate2 exhibited very low recovery (immobile fraction

= 0.9±0.3) (Extended Data Fig. 5a, Supplementary Video 7) indicative of very limited exchange of TFAM between the mt-nucleoid and the mitochondrial volume, and consistent with the very low concentration of free TFAM[37,38]. However, the ability of TFAM to rapidly diffuse within a nucleoid became evident when a bleached nucleoid fused with a neighboring unbleached nucleoid resulting in rapid exchange within the coalescing droplet (Fig. 4a,b, Supplementary Video 8). Furthermore, overexpression of TFAM-mKate2 to high levels in HeLa cells led to formation of enlarged nucleoids (~1 μm) (Extended Data Fig. 5e,f), and photobleaching a small spot ($R \approx 0.2\ \mu m$) within these structures (Fig. 4c, Supplementary Video 9) gave rise to recovery of ~70±20% of signal further indicating relatively high mobility of TFAM within mt-nucleoids (Fig. 4d). Based on observed recovery times of $\tau \sim 1$ min, we estimate diffusivities of $\sim 1 \times 10^{-3}\ \mu m^2/s$ (Fig. 4d), in line with our *in vitro* observations. Moreover, nucleoids larger than the diffraction limit exhibit clear liquid-like fusion behavior upon phototoxic and EtBr induced stress, consistent with a phase separation model (Extended Data Fig. 5h,i, Supplemental Movie 10), and exist as discrete structures in sporadically swollen mitochondria in HeLa cells (Fig. 4l). Furthermore, mt-nucleoids were largely unaffected upon swelling of mitochondria under hypo-osmotic conditions (Extended Data Fig. 5j,k), suggesting nucleoid components are not diffuse in the mitochondrial matrix, but that their size and shape of mt-nucleoids are intrinsic properties arising from phase separation. These dynamics and recovery features are comparable to the viscoelastic material properties of TFAM droplets *in vitro*.

To mimic the *in vitro* titration experiments of TFAM, we expressed TFAM-mKate2 and selected nucleoids with varying levels of expression for analysis using SIM (Fig. 4e; Extended Data Fig. 5m-o). Consistent with *in vitro* titration data, we find an increase of nucleoid sizes, reaching up to a few microns in length, resulting from increased TFAM-mKate2 expression levels. In addition, the mtDNA localization within these enlarged nucleoids had similar multiphase organization as observed in TFAM-mtDNA droplets *in vitro* (Fig. 4e; Extended Data Fig. 5m-o). This non-uniform structure is consistent with the layered organization deduced from biochemical analysis[39]. Moreover, labelling an additional

mitochondrial transcription factor, TFB2M, showed that it did not mix homogenously with TFAM and DNA, but had a preferential localization towards the mitochondrial inner membrane (Fig. 4f). The distinct localization of TFB2M reinforces that mt-nucleoids are complex, multi-component and multi-phase structures. To quantify the colocalization between pairs of these mt-nucleoid components, we used the Pearson's correlation coefficient as metric of partitioning within each microphase. TFAM has higher colocalization with mtDNA ($\rho_{TFAM,mtDNA}$ =0.6±0.1) than with TFB2M ($\rho_{TFAM,TFB2M}$ =0.3±0.1) (Fig. 4h). Furthermore, the correlation between TFAM and mtDNA is not 1, suggesting that there are microdomains that are enriched in TFAM, consistent with the *in vitro* multiphase behavior. To finally relate the *in vitro* behavior of mutant TFAM to its *in vivo* properties, we also examined a series of TFAM mutants in HeLa cells (Fig. 4g; Extended Data Fig. 5p-u). Notably, the HMGB+C-tail-mutant caused a complete inversion in localization of the mutant from the interior into the lining of the membrane ($\rho_{HMGB+C-tail,mtDNA}$ =0.2±0.1, $\rho_{HMGB+C-tail,TFB2M}$ =0.8±0.1) (Fig. 4h). This change in localization reflected differences in protein miscibility of HMGB+C-tail between the microphases, demonstrating that the HMGA and linker domains are important for association of TFAM with mtDNA. Other mutants also affected interactions between the mt-nucleoid components, although to a lesser extent. Specifically, the ΔC-tail mutant increased colocalization with mtDNA ($\rho_{\Delta C-tail,mtDNA}$=0.8±0.1), which suggests that loss of the C-tail increased affinity and binding of TFAM and mtDNA, while potentially competing for interactions with other proteins (Fig. 4h). Several other mutants also had increased affinities for TFB2M, albeit to a lesser extent as the HMGB+C-tail mutant, including the ΔHMGA mutant ($\rho_{\Delta HMGA,TFB2M}$=0.7±0.1), which approached HMGB+C-tail in composition (Fig. 4). Based on these results, we conclude that the *in vitro* properties of TFAM-mtDNA multiphase structures reflect the underlying physics of mitochondrial nucleoids *in vivo*.

To finally assess whether the phase-separation properties of mt-nucleoids are related to mitochondrial function, we measured mitochondrial activities in HGPS cells which are enriched for enlarged mt-nucleoids (Fig. 5). Single molecule FISH for mt-12S and mt-COI RNA demonstrated enrichment of mt-

RNA transcripts in enlarged nucleoids that were proportional to local TFAM levels (Fig. 5a-b, Extended Data Fig. 6a-f,m). RNA transcripts in enlarged mt-nucleoids localized along the perimeter of the mitochondrial membrane, but did not colocalize with nucleoids, suggesting that nucleoids and mt-RNA exist as distinct structures, and potentially immiscible phases, of (ribo)nucleoproteins (Fig. 5c-f), which is in line with the weak partitioning and weak effect on morphology of RNA relative to DNA on TFAM droplets in the *in vitro* system (Extended Data Fig. 4d-u). Similar increased transcriptional activity of enlarged mt-nucleoids was evident when nascent transcription was measured by using BrU incorporation (Extended Data Fig. 6g-l,n). Consistently, we did not observe changes in mt-RNA transcripts on a population level as measured by qPCR, which supports that enlarged nucleoids remain transcriptionally active, also in line with RNA-FISH imaging (Extended Data Fig. 6o). However, the enrichment of enlarged phase-separated mt-nucleoids in HGPS was associated with altered mitochondrial metabolic functions (Fig. 5g). Basal mitochondrial respiration, maximal respiration and reserve capacity were reduced in HGPS fibroblasts containing enlarged mt-nucleoids compared to isogenic non-affected fibroblasts (Fig. 5h-j), indicating functional impairment of mitochondrial oxidative phosphorylation and ATP regeneration. Furthermore, HGPS fibroblasts from older affected donors had elevated mitochondrial ROS and membrane potential compared to young HGPS or unaffected proband control fibroblasts (Fig. 5k,l). These observations demonstrate that the presence of enlarged mt-nucleoids generated by phase separation is accompanied by mitochondrial dysfunction.

Our results show that mitochondrial nucleoids form by phase separation. Considering the recent evidence for a role of phase separation in the formation of nuclear DNA and chromatin domains, including heterochromatin[29-32], our observations point to a broad role of phase separation in organizing DNA. Since mitochondria are derived from prokaryotes, which arrange their DNA into analogous nucleoids, phase separation may be an evolutionarily conserved mechanism for the organization of genetic material. In support, bacterial nucleoids have been described to behave as fluids[40], and some bacterial nucleoprotein complexes also undergo liquid-liquid phase separation[41]. Moreover, mitochondrial nucleoids may not be

the only example of phase separation within the mitochondria, as mitochondria have also been reported to contain various RNA granules[42,43].

Our mutational analysis of the major mt-nucleoid protein TFAM suggests a model in which weak interactions along the flexible backbone of TFAM promote phase separation, and in the presence of DNA, the HMG domains of TFAM each bind DNA by intercalating into the helical strand, and together, further bend and stabilize the DNA fiber (Extended Data Fig. 4b)[34,35]. While the ability of TFAM to bind DNA is well characterized[8,44,45], binding alone does not explain the higher-order structural features of mt-nucleoids such as their observed uniform size and shape, and their dynamic emergent properties, including liquid-like fusion events and internal rearrangements. Our findings demonstrate that individual TFAM molecules have a propensity for self-assembly into a separate protein-rich phase within mt-nucleoids, generating a gel-like polymer meshwork that constitutes a nucleoid matrix. Full length TFAM has unequal solubilities with nucleoid components (mtDNA, TFB2M), thereby generating microphases within the mt-nucleoid droplet. Our observation that truncation and modification of TFAM domains can lead to pronounced changes in localization within the nucleoid droplet underscores how TFAM-specific interactions can independently confer miscibility and significantly alter nucleoid structure. This physical model supports a platform for other known mt-nucleoid associated proteins to partition into these dynamic, yet persistent, structures[39]. Importantly, the phase behavior of TFAM and mtDNA accounts for the observed morphological features of mt-nucleoids as discrete, non-membranous entities within mitochondria, their viscoelastic dynamics *in vivo*, and their ability to reach sizes larger than 100 nm as observed in HGPS cells. This physical, phase separation model complements previous self-assembly studies of TFAM and mtDNA into nucleoid-like structures under dilute conditions[8,44,45], by extending them to reveal the importance of protein-protein interactions in driving the self-assembly of the mitochondrial genome. Our results finally suggest that phase separation properties are linked to mitochondrial function, including transcription and metabolic activity. One intriguing possibility is that phase separation may have a protective function by forming a proteinaceous layer around mtDNA to

prevent the deterioration of the mitochondrial genome as observed in aging. Taken together, our observations suggest that phase separation is an evolutionarily conserved mechanism for nucleoid biogenesis and that the physical properties of nucleoids are essential to ensure mitochondrial function.

References:

1 Gustafsson, C. M., Falkenberg, M. & Larsson, N.-G. Maintenance and expression of mammalian mitochondrial DNA. *Annual Review of Biochemistry* **85**, 133-160 (2016).

2 Chen, X. J. & Butow, R. A. The organization and inheritance of the mitochondrial genome. *Nature Reviews Genetics* **6**, 815 (2005).

3 Kukat, C. & Larsson, N.-G. mtDNA makes a U-turn for the mitochondrial nucleoid. *Trends in Cell Biology* **23**, 457-463 (2013).

4 Kukat, C. *et al.* Super-resolution microscopy reveals that mammalian mitochondrial nucleoids have a uniform size and frequently contain a single copy of mtDNA. *Proceedings of the National Academy of Sciences* **108**, 13534-13539 (2011).

5 Brown, T. A. *et al.* Superresolution fluorescence imaging of mitochondrial nucleoids reveals their spatial range, limits, and membrane interaction. *Molecular and Cellular Biology* **31**, 4994-5010 (2011).

6 Brewer, L. R. *et al.* Packaging of single DNA molecules by the yeast mitochondrial protein Abf2p. *Biophysical Journal* **85**, 2519-2524 (2003).

7 Kaufman, B. A. *et al.* The mitochondrial transcription factor TFAM coordinates the assembly of multiple DNA molecules into nucleoid-like structures. *Molecular Biology of the Cell* **18**, 3225-3236 (2007).

8 Kukat, C. *et al.* Cross-strand binding of TFAM to a single mtDNA molecule forms the mitochondrial nucleoid. *Proceedings of the National Academy of Sciences* **112**, 11288-11293 (2015).

9 Balaban, R. S., Nemoto, S. & Finkel, T. Mitochondria, oxidants, and aging. *Cell* **120**, 483-495 (2005).

10 Sun, N., Youle, R. J. & Finkel, T. The mitochondrial basis of aging. *Molecular Cell* **61**, 654-666 (2016).

11 Cadenas, E. & Davies, K. J. Mitochondrial free radical generation, oxidative stress, and aging. *Free Radical Biology and Medicine* **29**, 222-230 (2000).

12 Yakes, F. M. & Van Houten, B. Mitochondrial DNA damage is more extensive and persists longer than nuclear DNA damage in human cells following oxidative stress. *Proceedings of the National Academy of Sciences* **94**, 514-519 (1997).

13 Bratic, A. & Larsson, N.-G. The role of mitochondria in aging. *The Journal of Clinical Investigation* **123**, 951-957 (2013).

14 Trifunovic, A. *et al.* Premature ageing in mice expressing defective mitochondrial DNA polymerase. *Nature* **429**, 417 (2004).

15 Kujoth, G. C. *et al.* Mitochondrial DNA Mutations, Oxidative Stress, and Apoptosis in Mammalian Aging. *Science* **309**, 481-484 (2005).

16 Gordon, L. B., Rothman, F. G., López-Otín, C. & Misteli, T. Progeria: a paradigm for translational medicine. *Cell* **156**, 400-407 (2014).

17 Xiong, Z. M. *et al.* Methylene blue alleviates nuclear and mitochondrial abnormalities in progeria. *Aging Cell* **15**, 279-290 (2016).

18 Rivera-Torres, J. *et al.* Identification of mitochondrial dysfunction in Hutchinson–Gilford progeria syndrome through use of stable isotope labeling with amino acids in cell culture. *Journal of Proteomics* **91**, 466-477 (2013).
19 Legros, F., Malka, F., Frachon, P., Lombès, A. & Rojo, M. Organization and dynamics of human mitochondrial DNA. *Journal of Cell Science* **117**, 2653-2662 (2004).
20 Ashley, N. & Poulton, J. Anticancer DNA intercalators cause p53-dependent mitochondrial DNA nucleoid re-modelling. *Oncogene* **28**, 3880 (2009).
21 Minamikawa, T. *et al.* Chloromethyl-X-rosamine (MitoTracker Red) photosensitises mitochondria and induces apoptosis in intact human cells. *Journal of Cell Science* **112**, 2419-2430 (1999).
22 Shin, Y. & Brangwynne, C. P. Liquid phase condensation in cell physiology and disease. *Science* **357**, eaaf4382 (2017).
23 Hyman, A. A., Weber, C. A. & Jülicher, F. Liquid-liquid phase separation in biology. *Annual Review of Cell and Developmental Biology* **30**, 39-58 (2014).
24 Banani, S. F., Lee, H. O., Hyman, A. A. & Rosen, M. K. Biomolecular condensates: organizers of cellular biochemistry. *Nature Reviews Molecular Cell Biology* **18**, 285 (2017).
25 Feric, M. *et al.* Coexisting liquid phases underlie nucleolar subcompartments. *Cell* **165**, 1686-1697 (2016).
26 Brangwynne, C. P., Mitchison, T. J. & Hyman, A. A. Active liquid-like behavior of nucleoli determines their size and shape in Xenopus laevis oocytes. *Proceedings of the National Academy of Sciences* **108**, 4334-4339 (2011).
27 Brangwynne, C. P. *et al.* Germline P granules are liquid droplets that localize by controlled dissolution/condensation. *Science* **324**, 1729-1732 (2009).
28 Molliex, A. *et al.* Phase separation by low complexity domains promotes stress granule assembly and drives pathological fibrillization. *Cell* **163**, 123-133 (2015).
29 Strom, A. R. *et al.* Phase separation drives heterochromatin domain formation. *Nature* **547**, 241 (2017).
30 Larson, A. G. *et al.* Liquid droplet formation by HP1α suggests a role for phase separation in heterochromatin. *Nature* **547**, 236 (2017).
31 Gibson, B. A. *et al.* Organization of Chromatin by Intrinsic and Regulated Phase Separation. *Cell* (2019).
32 Sanulli, S. *et al.* HP1 reshapes nucleosome core to promote phase separation of heterochromatin. *Nature* **575**, 390-394 (2019).
33 Sabari, B. R. *et al.* Coactivator condensation at super-enhancers links phase separation and gene control. *Science*, eaar3958 (2018).
34 Rubio-Cosials, A. *et al.* Human mitochondrial transcription factor A induces a U-turn structure in the light strand promoter. *Nature Structural Molecular Biology* **18**, 1281 (2011).
35 Ngo, H. B., Kaiser, J. T. & Chan, D. C. The mitochondrial transcription and packaging factor TFAM imposes a U-turn on mitochondrial DNA. *Nature Structural Molecular Biology* **18**, 1290 (2011).
36 Lin, Y., Protter, D. S., Rosen, M. K. & Parker, R. Formation and maturation of phase-separated liquid droplets by RNA-binding proteins. *Molecular Cell* **60**, 208-219 (2015).
37 Lu, B. *et al.* Phosphorylation of human TFAM in mitochondria impairs DNA binding and promotes degradation by the AAA+ Lon protease. *Molecular Cell* **49**, 121-132 (2013).
38 Matsushima, Y., Goto, Y.-i. & Kaguni, L. S. Mitochondrial Lon protease regulates mitochondrial DNA copy number and transcription by selective degradation of mitochondrial transcription factor A (TFAM). *Proceedings of the National Academy of Sciences* **107**, 18410-18415 (2010).
39 Bogenhagen, D. F., Rousseau, D. & Burke, S. The layered structure of human mitochondrial DNA nucleoids. *Journal of Biological Chemistry* **283**, 3665-3675 (2008).
40 Cunha, S., Woldringh, C. L. & Odijk, T. Polymer-mediated compaction and internal dynamics of isolated Escherichia coli nucleoids. *Journal of Structural Biology* **136**, 53-66 (2001).

41 Monterroso, B. *et al.* Bacterial FtsZ protein forms phase separated condensates with its nucleoid associated inhibitor SlmA. *EMBO Reports* **20** (2019).
42 Jourdain, A. A., Boehm, E., Maundrell, K. & Martinou, J.-C. J. J. C. B. Mitochondrial RNA granules: compartmentalizing mitochondrial gene expression. *Journal of Cell Biology* **212**, 611-614 (2016).
43 Jourdain, A. A. *et al.* GRSF1 regulates RNA processing in mitochondrial RNA granules. *Cell Metabolism* **17**, 399-410 (2013).
44 Farge, G. *et al.* In vitro-reconstituted nucleoids can block mitochondrial DNA replication and transcription. *Cell Reports* **8**, 66-74 (2014).
45 Wong, T. S. *et al.* Biophysical characterizations of human mitochondrial transcription factor A and its binding to tumor suppressor p53. *Nucleic Acids Research* **37**, 6765-6783 (2009).

Acknowledgements

We thank the members of the Misteli lab for discussion and experimental design; L. Schiltz and A. Schibler for initial help with protein purification; J. Jones and M. Taylor for help with final protein expression and purification at the NIH/NCI/CCR Protein Production Core; T. Karpova and D. Ball for help with Structured Illumination Microscopy and Laser Scanning Confocal Microscopy as part of the NIH/NCI/CCR LRBGE Optical Imaging Core; G. Pegoraro and L. Ozbun for help with high throughput imaging and automated liquid handling at the NIH/NCI/CCR High Throughput Imaging Facility (HiTIF); and K. M. McKinnon for help with cell sorting as part of the NIH/NCI/CCR FACS Core Facility.

Funding: Research in the Misteli lab was supported by funding from the Intramural Research Program of the National Institutes of Health (NIH), National Cancer Institute, and Center for Cancer Research (1-ZIA-BC010309); MF is supported by a Postdoctoral Research Associate Training (PRAT) fellowship from the National Institute of General Medical Sciences (NIGMS, 1Fi2GM128585-01); TD, JT, DC, and VB are supported by the NIA Intramural Research Program of the NIH (AG000727).

Author contributions

MF performed live/fixed cell microscopy and *in vitro* experiments and analysis. TD, JT, and DC performed and analyzed mitochondrial Seahorse assays, mitochondrial membrane potential and mitochondrial ROS measurements on normal and HGPS cells. TM and MF planned experiments, discussed results, and wrote the manuscript. All authors revised the manuscript. **Competing interests:**

Authors declare no competing interests. **Data availability:** All data are in the main text or the supplementary materials and can be available from the corresponding author on request.

Supplementary Information

Methods

References

Extended Data Table 1

Extended Data Figures 1-6

Supplementary Videos 1-10

Figure Legends

Figure 1:

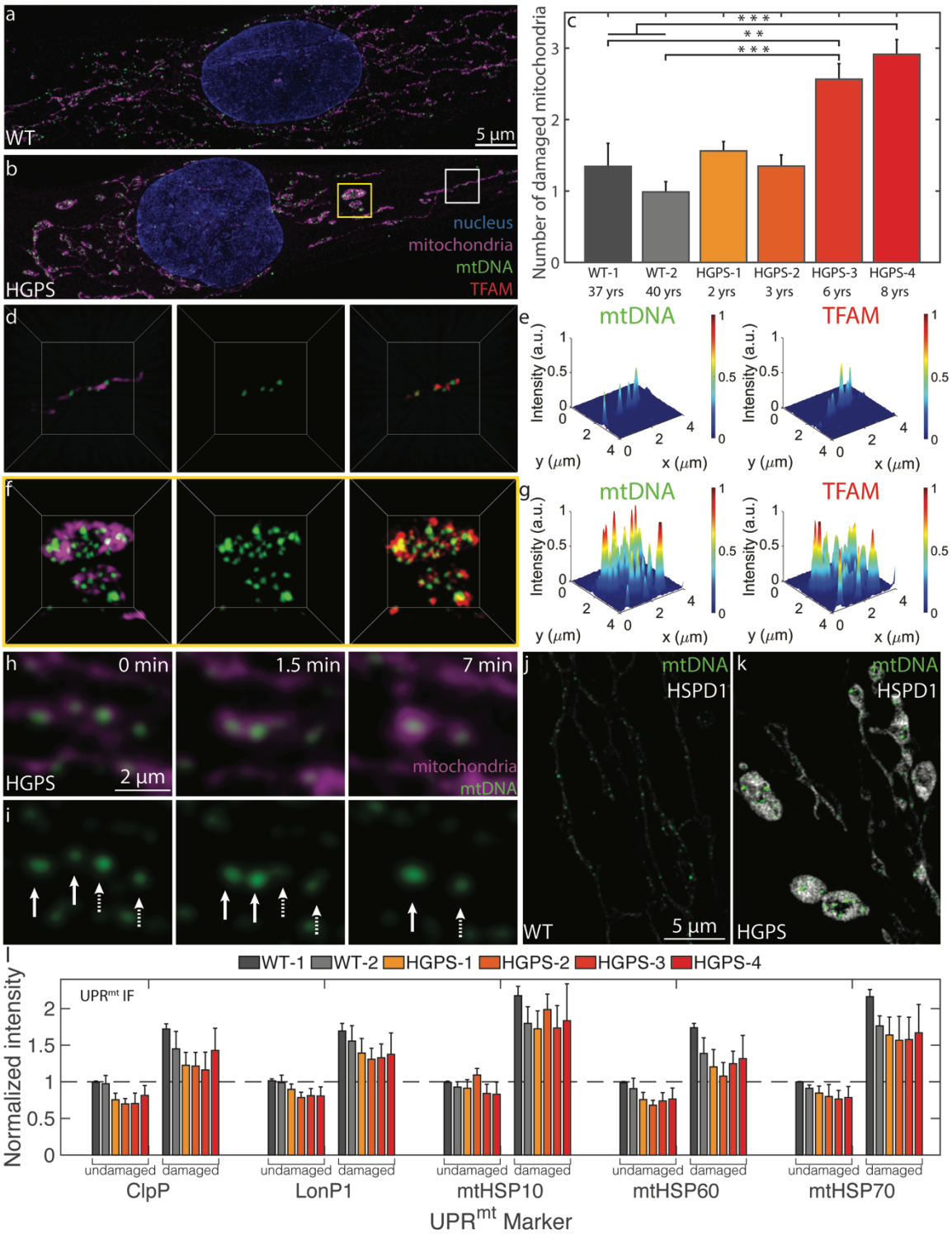

Figure 1: Enlarged mitochondrial nucleoids are prominent in a premature aging disease and can also arise from liquid-like fusion events under stress. a,b, Maximum intensity projections of SIM images of a fixed normal (**a**) and an HGPS (**b**) human skin fibroblast, where the mitochondria are labelled in magenta with MitoTracker Red, mtDNA nucleoids in green with anti-DNA, and the nucleus in blue with DAPI. Scale bar = 5 µm. **c**, Bar graph quantifying the number of damaged mitochondria per cell based on high-throughput imaging of two wild-type and four HGPS primary skin fibroblast cell lines. Error bars represent averages ±SEM for n=3 experimental replicates (each experimental replicate had 15 technical replicates each containing 5 fields of view, approximately 2,000-5,000 total cells for each cell line analyzed), where p-value for the ANOVA test statistic was $p<0.001$. For individual pairs, $^{**}p<0.01$, $^{***}p<0.001$. **d,f**, Three-dimensional views of normal mitochondria (**d**) annotated by white box in **b** and swollen mitochondria (**f**) annotated by yellow box in **b** and showing TFAM localization in red with anti-TFAM); the length of the box = 4 µm. **e,g**, Normalized intensity distributions of nucleoids labelled with anti-DNA and with anti-TFAM corresponding to images from **d** and **f**, respectively. **h,i**, Time-course experiment of live HGPS cells under photo-toxic conditions. Mitochondria were labelled with MitoTracker Deep Red (**h**, magenta) and mtDNA was labelled with PicoGreen (**h,i,** green). Scale bar = 2 µm. Arrow heads indicate pairs of nucleoids that undergo liquid-like fusion events. **j,k**, Single z-slices of SIM images of UPR^{mt} in mitochondria from fixed normal (**j**) and an HGPS (**k**) human skin fibroblast, where the UPR^{mt} marker is gray-scale with anti-HSPD1 (mtHSP60), and mtDNA nucleoids are in green with anti-DNA. Scale bar = 5 µm. **o**, Immunofluorescence quantification of UPR^{mt} markers (ClpP, LonPI, mtHSP10, mtHSP60, mtHSP70) in all six primary cell lines reported as normalized intensity values in undamaged and damaged mitochondria from high-throughput confocal images, where n=3 independent experimental replicates (each experimental replicate, containing three technical replicates, had a total of 150-600 cells for each cell line and UPR^{mt} marker) and error bars are standard error.

Figure 2:

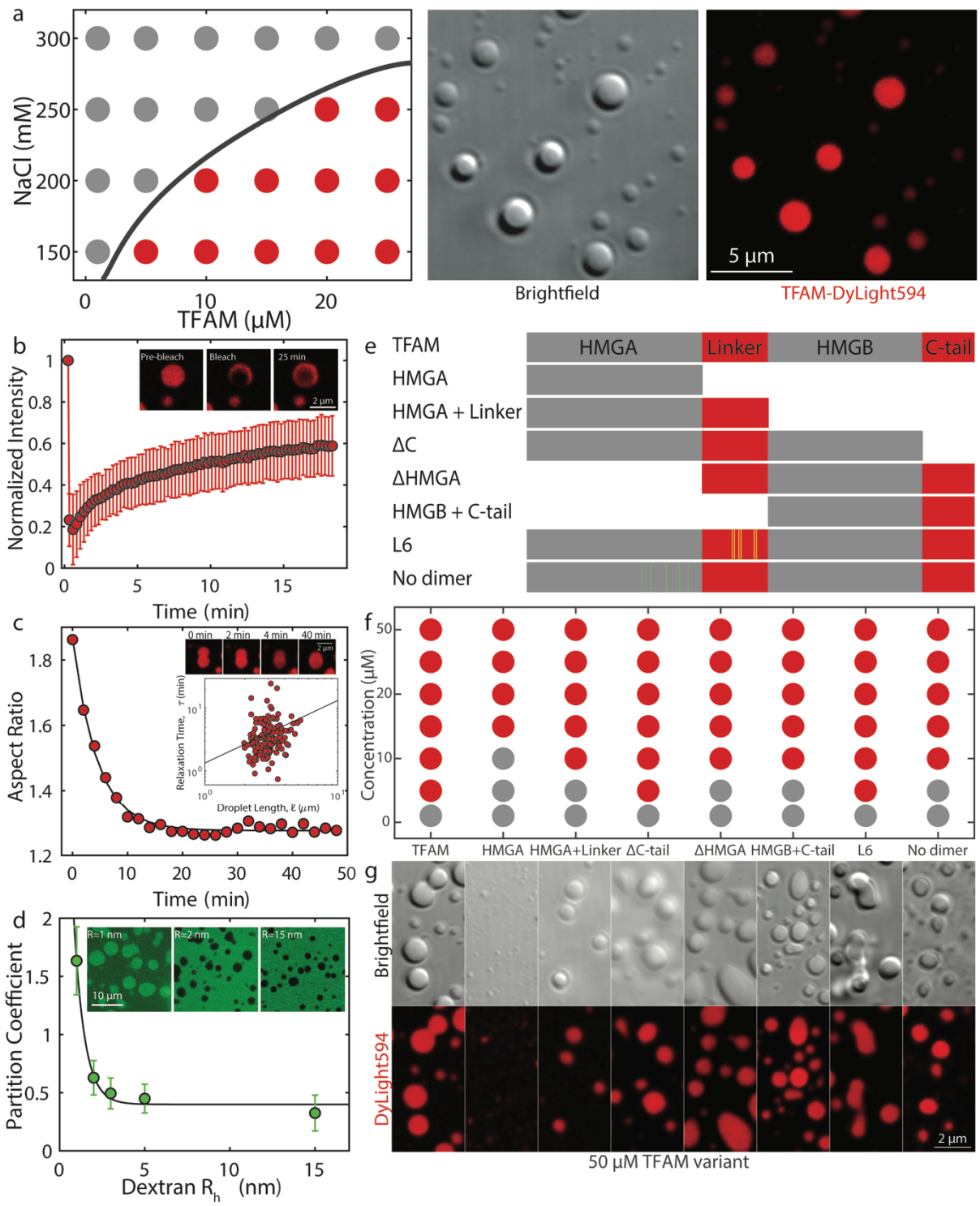
a
NaCl (mM)
TFAM (μM)
Brightfield
5 μm
TFAM-DyLight594
b
Normalized Intensity
Time (min)
Pre-bleach
Bleach
25 min
2 μm
c
Aspect Ratio
Time (min)
0 min
2 min
4 min
40 min
Relaxation Time, τ (min)
Droplet Length, ℓ (μm)
d
Partition Coefficient
Dextran R_h (nm)
R≈1 nm
R≈2 nm
R≈15 nm
10 μm
e
TFAM
HMGA
Linker
HMGB
C-tail
HMGA
HMGA + Linker
ΔC
ΔHMGA
HMGB + C-tail
L6
No dimer
f
Concentration (μM)
TFAM
HMGA
HMGA+Linker
ΔC-tail
ΔHMGA
HMGB+C-tail
L6
No dimer
g
Brightfield
DyLight594
2 μm
50 μM TFAM variant

Figure 2: TFAM phase separates into viscoelastic droplets, driven by multivalent interactions. a, Phase diagram of TFAM under various protein and salt concentrations, where grey dots indicate single/soluble phase, red dots signify two phases/droplets present. DIC image (top) and maximum intensity projection (bottom) of TFAM-DyLight594 droplets at 25 μM and 150 mM NaCl in 20 mM Tris-HCl, pH 7.5 thirty minutes after mixing. Scale bar = 5 μm. **b**, FRAP using 488 and 561 nm light performed on a ~1 μm spot on TFAM droplet thirty minutes after mixing. Inset shows representative fluorescent image of TFAM-DyLight594 pre-bleach, immediately post-bleach, and 25 minutes post-bleach. Scale bar = 2 μm. Values represent averages ± SD from n = 15 droplets. **c**, Aspect ratio of droplet shape as a function of time after contact for a representative droplet. Top inset shows fusion images corresponding to the trace at t = 0, 2, 4 and 40 mins. Scale bar = 2 μm. Bottom inset shows data for all droplets analyzed (n= 3 experimental replicates, where ~50 droplets analyzed per experiment) of characteristic relaxation times as a function of droplet size. Solid line is the linear fit, where the slope is a measure of the inverse capillary velocity. **d**, The partition coefficient of dextran-FITC into TFAM droplets as a function of dextran average hydrodynamic radius estimated from the molecular weight. Inset shows representative images showing localization of dextran-FITC for $R_h \approx 1$, 2 and 25 nm. Scale bar = 10 μm. Values represent averages ± SD from n = 3 experiments (>20 droplets analyzed per condition for each experiment). **e**, Schematic diagram of mutants with HMG domains in grey and intrinsically disordered regions in red. Yellow and green lines indicate point mutations in L6 and no dimer mutants, respectively. **f**, Phase diagram of mutants at 150 mM NaCl and 20 mM Tris-HCl, pH 7.5 for a range of protein concentrations. **g**, Fluorescent maximum intensity projections of mutants at 50 μM protein and 150 mM NaCl, 20 mM Tris-HCl, pH 7.5 within 30-60 minutes after mixing. Scale bar = 2 μm.

Figure 3:

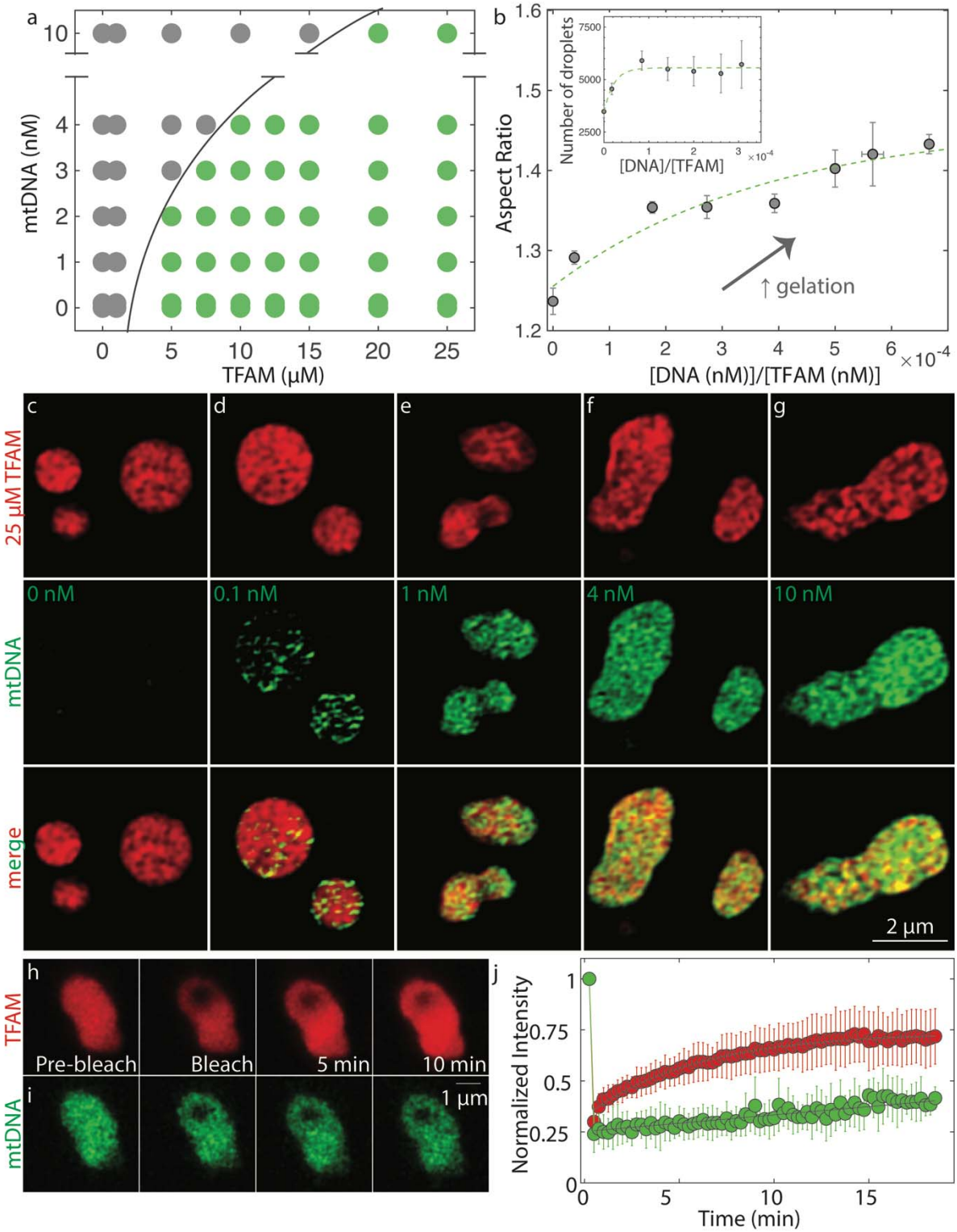
a
mtDNA (nM)
TFAM (μM)
b
Aspect Ratio
Number of droplets
[DNA]/[TFAM]
↑ gelation
[DNA (nM)]/[TFAM (nM)]
25 μM TFAM
mtDNA
merge
0 nM
0.1 nM
1 nM
4 nM
10 nM
2 μm
TFAM
mtDNA
Pre-bleach
Bleach
5 min
10 min
1 μm
Normalized Intensity
Time (min)

Figure 3: Formation of TFAM-mtDNA multiphase, gel-like structures. a, Phase diagram of mtDNA versus TFAM denoting single/soluble phase (gray) or two phases/droplets (green). Each point on the phase diagram representing a unique DNA and protein concentration was measured from n=2-12 independent experiments. Black solid line delineates deduced phase boundary. **b**, Aspect ratio as a function of dimensionless concentration (molar concentration DNA/molar concentration TFAM). Values represent binned conditions from DNA/TFAM conditions measured in (**a**) and error bars are SEM. Inset: number of TFAM-mtDNA droplets per field of view as a function of dimensionless concentration. Values represent binned conditions from DNA/TFAM conditions measured in (**a**) and error bars are SEM. **c-g**, SIM images of droplets thirty minutes after mixing with various amounts of mtDNA: 0 nM (**c**), 0.1 nM (**d**), 1 nM (**e**), 4 nM (**f**), and 10 nM (**g**). Top row is of TFAM-DyLight594 (red), middle row is of mtDNA-Alexa488 (green) and bottom row is the merged image. Scale bar = 2 μm. **h-j**, FRAP experiments on TFAM-mtDNA droplets at 25 μM TFAM (**h**, red) and 10 nM mtDNA (**i**, green). **j**, FRAP recovery curve showing intensity as a function of time for TFAM (red) and mtDNA (green). Values represent averages ± SD from n = 16 droplets.

Figure 4:

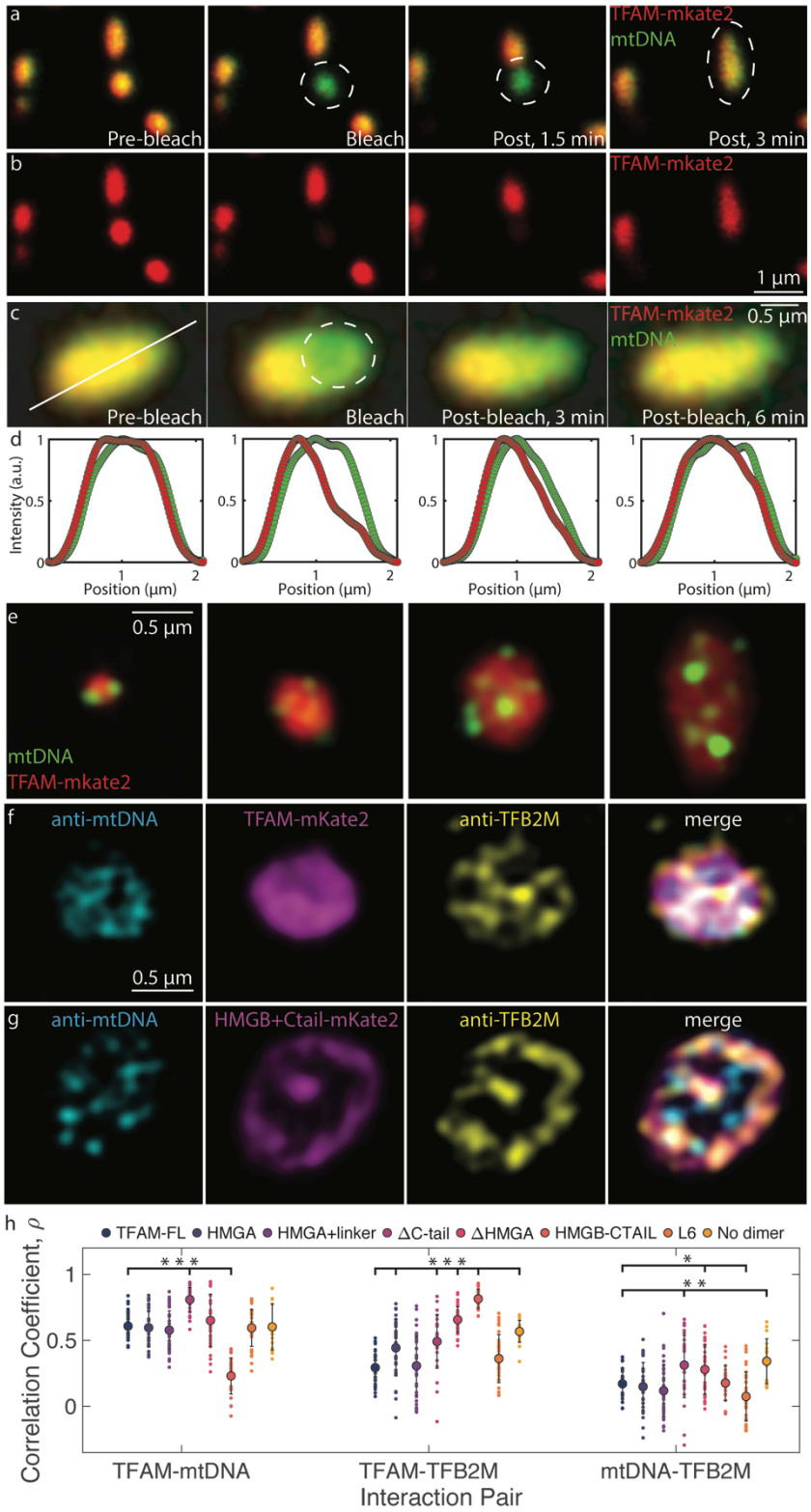
a
Pre-bleach
Bleach
Post, 1.5 min
TFAM-mkate2
mtDNA
Post, 3 min
b
TFAM-mkate2
1 µm
c
Pre-bleach
Bleach
Post-bleach, 3 min
TFAM-mkate2
mtDNA
0.5 µm
Post-bleach, 6 min
d
Intensity (a.u.)
Position (µm)
e
0.5 µm
mtDNA
TFAM-mkate2
f
anti-mtDNA
TFAM-mKate2
anti-TFB2M
merge
0.5 µm
g
anti-mtDNA
HMGB+Ctail-mKate2
anti-TFB2M
merge
h
TFAM-FL
HMGA
HMGA+linker
ΔC-tail
ΔHMGA
HMGB-CTAIL
L6
No dimer
Correlation Coefficient, ρ
TFAM-mtDNA
TFAM-TFB2M
mtDNA-TFB2M
Interaction Pair

Figure 4: Phase separation behavior of TFAM in live cells. a,b, FRAP experiment performed on a small nucleoid that later undergoes a fusion event in live HeLa cells expressing TFAM-mKate2. **a**, The overlay of TFAM-mKate2 (red) and of mtDNA labelled with PicoGreen (green) pre-bleach, bleach, 1.5 minutes and 3 minutes post-bleach, and **b**, the single-channel of TFAM-mKate2 (red). Scale bar = 1 µm. **c,d**, FRAP experiment performed on an enlarged nucleoid in live HeLa cells expressing TFAM-mKate2 (n = 18 cells), where (**c**) is the overlay of TFAM-mKate2 (red) and of mtDNA labelled with PicoGreen (green) pre-bleach, bleach, 3 minutes and 6 minutes post-bleach. The solid white line indicates the pixels that were analyzed for intensity. The dashed white circle denotes the part of the nucleoid that was bleached. Scale bar = 0.5 µm. **d**, The normalized intensity of TFAM-mKate2 (red) and PicoGreen (green) where the x-axis corresponds to the solid white line from (**c**). **e**, Single z-slices of SIM merged images of nucleoids ranging in size after overexpression of TFAM-mKate2 in a fixed HeLa cell, where mtDNA (green, anti-DNA), and TFAM (red, TFAM-mKate2). Scale bar = 0.5 µm. **f**,**g**, Single z-slices of SIM individual channels of fixed HeLa cells after TFAM-mKate2 (**f**) and HMGB+C-tail-mKate2 (**g**) overexpression (magenta), where mtDNA is labelled with anti-mtDNA (cyan) and TFB2M is labelled with anti-TFB2M (yellow). Merged images are shown as an overlay of all three channels. Scale bar = 0.5 µm. **h**, Colocalization of channels is shown computed from Pearson's correlation coefficient for each interaction pair shown for TFAM-FL and all TFAM mutant constructs overexpressed in HeLa cells (n=20-40 nucleoids from 4-5 cells imaged for each mutant construct). ANOVA analysis shows statistical significance across all groups, where $p<2e-16$ for TFAM-mtDNA interactions, $p<2e-16$ for TFAM-TFB2M interactions, and $p = 1.3e-8$ for mtDNA-TFB2M interactions. Notation on graph denotes statistical analysis relative to TFAM-FL, where $*p<0.05$, $**p<0.01$, and $***p<0.001$.

Figure 5:

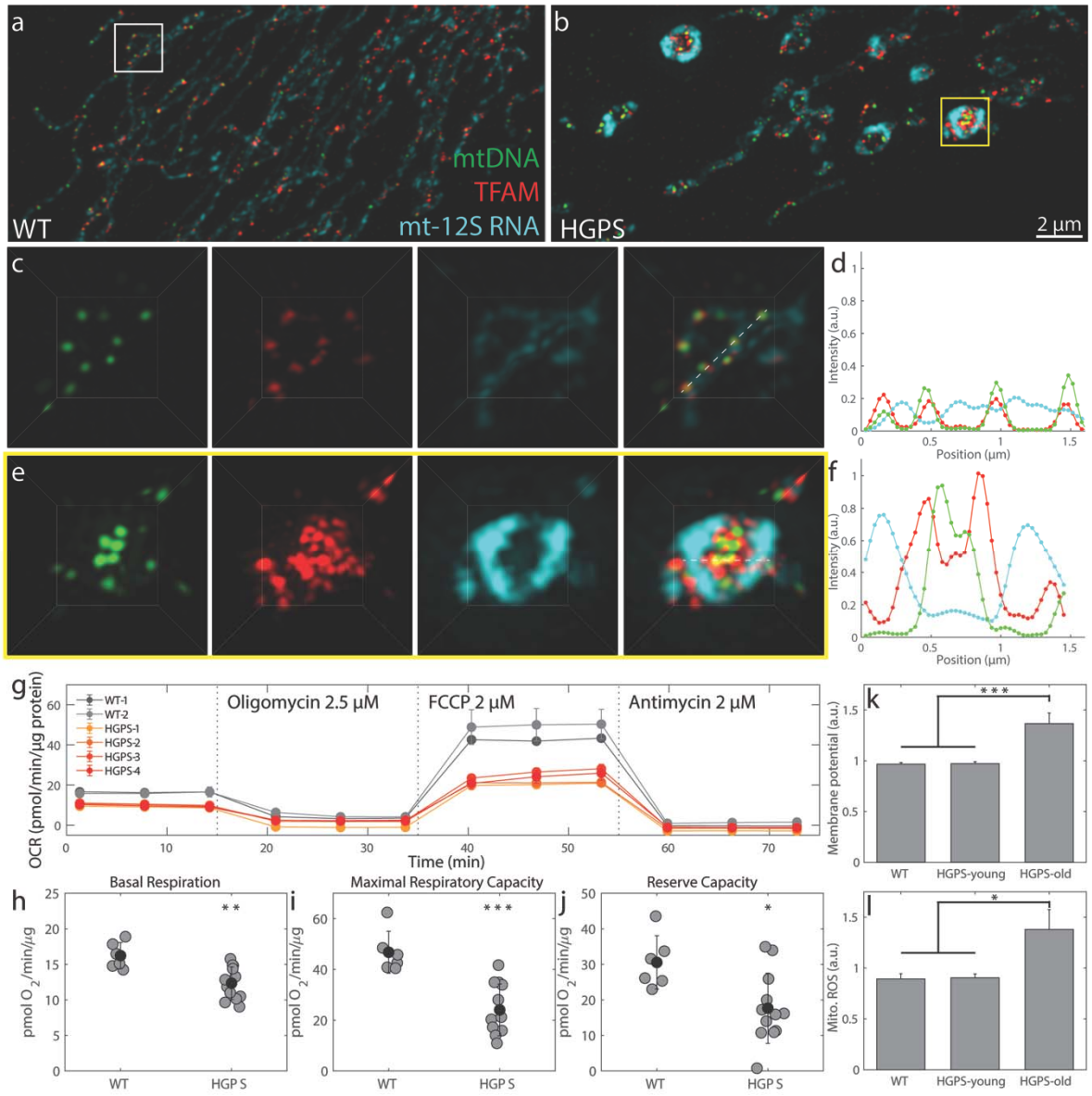
a
b
mtDNA
TFAM
mt-12S RNA
WT
HGPS
2 µm
c
d
e
f
Intensity (a.u.)
Position (µm)
g
WT-1
WT-2
HGPS-1
HGPS-2
HGPS-3
HGPS-4
Oligomycin 2.5 µM
FCCP 2 µM
Antimycin 2 µM
OCR (pmol/min/µg protein)
Time (min)
k
Membrane potential (a.u.)
WT
HGPS-young
HGPS-old
h
Basal Respiration
i
Maximal Respiratory Capacity
j
Reserve Capacity
pmol O2/min/µg
HGP S
l
Mito. ROS (a.u.)

Figure 5: Functional features of enlarged mt-nucleoids. a,b, Maximum intensity projections of SIM images of a fixed normal (**a**) and an HGPS (**b**) human skin fibroblast, where mtDNA is in green with anti-DNA, TFAM is in red with anti-TFAM, and mt-12S RNA FISH is in cyan. Scale bar = 2 µm. **c,e**, Three-dimensional views of normal mitochondria (**c**) annotated by white box in **a** and swollen mitochondria (**e**) annotated by yellow box in **b** and showing individual channels and an overlay; box ≈ 2.5 x 3 µm. **d,f**, Normalized intensity distributions of nucleoids labelled with anti-DNA (green), anti-TFAM (red), and mt-12S RNA (cyan) corresponding to images from **c** and **e**, respectively. **g-j**, Seahorse assay results on primary skin fibroblasts from wildtype cell lines (WT-1,2) and HGPS cell lines (HGPS-1,2,3,4) from a representative experiment. **g**, The oxygen consumption rate (OCR) as a function of time after perturbation with oligomycin, 2.5 µM at t = 16 minutes, FCCP at 2 µM, at t = 24 minutes, and antimycin 2 µM at t = 55 minutes. Representative trace from a single experiment, error bars are SEM of technical replicates (n=3). Averaged results for WT and HGPS cells pooled together: basal respiration (**h**), maximal respiratory capacity (**i**), and reserve capacity (**j**). Error bars are standard deviation, where *$p<0.05$, **$p<0.01$ and ***$p<0.001$. For (**g**), three experimental replicates were performed, and for (**h-j**) experiments were pooled among cell types, where values represent averages ± SD from n = 6 independent experimental replicates of WT cells and n = 12 independent experimental replicates of HGPS cells. **k**, Mitochondrial membrane potential using TMRM. Cells were grouped as WT (n=8 independent measurements), HGPS young (n=8 independent measurements), and HGPS old (n=8 independent measurements). Error bars are SEM, where p-value for the ANOVA test statistic was $p<0.001$. For individual pairs, ***$p<0.001$. **l**, Mitochondrial ROS using MitoSOX Red. Cells were grouped as WT (n=6 independent measurements), HGPS young (n=6 independent measurements), and HGPS old (n=6 independent measurements). Error bars are SEM, where p-value for the ANOVA test statistic was $p<0.05$. For individual pairs, *$p<0.05$.